A comparative STM and SPA-LEED study on the evolution of strain induced stripe pattern on Cu/Ni(100)

L. Nedelmann [a], B. Müller [a,*], B. Fischer [a], K. Kern [a], D. Erdös [b], J. Wollschläger [b], M. Henzler [b]

[a] *Institut de Physique Expérimentale, EPF Lausanne, CH-1015 Lausanne, Switzerland*
[b] *Institut für Festkörperphysik, Universität Hannover, D-30167 Hannover, Germany*

Abstract

The epitaxial growth of Cu multilayers on Ni(100) is investigated by high-resolution LEED and variable temperature STM. Particular emphasis is put on the quantitative characterization of the recently discovered strain relief mechanism via internal {111} faceting. This mechanism is associated with the occurrence of patterns of orthogonal stripes at the film surface. The complementarity of real space and reciprocal space techniques are used to determine quantities such as stripe height, width and density with high accuracy. The pros and cons of local real space and integral reciprocal space techniques are discussed in detail. © 1997 Elsevier Science B.V. All rights reserved.

Keywords: Copper; Low energy electron diffraction; Molecular beam epitaxy; Nickel; Scanning tunneling microscopy; Surface stress; Surface structure, morphology, roughness and topography

1. Introduction

Molecular beam epitaxy (MBE) is a versatile technique for the growth of thin epitaxial films of metals, semiconductors and insulators. The detailed control of the growth conditions (e.g. deposition flux, substrate temperature) allows the fabrication of epitaxial structures with precision on the atomic layer level. In most applications, MBE is a nonequilibrium process and the growth is mainly governed by the kinetics of the involved surface processes such as sticking, diffusion, nucleation and aggregation [1]. In addition, in hetero-

epitaxial growth, i.e. substrate and deposit consist of different species, strain effects due to the structural misfit are of crucial importance. In many systems, strained epitaxial films tend initially to grow as pseudomorphic islands and layers before, at a critical thickness, strain relaxation through introduction of defects or morphology changes is observed [2–7]. The strain relief scenarios play a very important role in heteroepitaxial growth, because they determine to a large extent surface morphology and film quality.

Recently, we have reported a novel strain relief mechanism which has been found for the growth of Cu layers on Ni(100). The mechanism is associated with the occurrence of orthogonal stripes and is operative from submonolayer coverage [8,9]. Here, we present a comprehensive, quantitative

---

* Corresponding author. Fax: +41 21 6933604;
e-mail: bert.mueller@pe.dp.epfl.ch

investigation of stripe formation and growth by means of scanning tunneling microscopy (STM) and high-resolution low energy electron diffraction (SPA-LEED). Thus, a local, real space and an integral, reciprocal space technique are combined to extract quantities such as stripe density, height and width with high precision. Cu/Ni(100) is especially suitable for a comparison between these two powerful surface sensitive tools, because the system grows two-dimensionally [8–11], so that complications of the analysis by islands are avoided.

2. Experimental

STM measurements were performed in an ultra-high vacuum chamber (base pressure: 2×10^{-10} mbar) by means of variable temperature STM ($T = 25...800$ K). Similar instrumentation is described in Ref. [12]. The STM images were recorded in the constant current mode, at typical tunneling currents of 2–10 nA and bias voltages of 0.5–1.5 V. The nickel crystal was cleaned by argon ion sputtering alternately performed at elevated ($T_s = 550$ K) and room temperature and subsequent annealing to 1400 K. This treatment results in nearly perfect terraces of several hundred nanometers. Impurities such as oxygen or carbon were below the detection limit of Auger spectroscopy. Copper was deposited by thermal evaporation at growth rates between 5×10^{-3} and 1×10^{-2} monolayers per second (ML s^{-1}).

For the SPA-LEED experiments performed in a different UHV chamber (base pressure: 5×10^{-11} mbar) [13], the same preparation procedure was employed. A constant growth rate of $(5.0 \pm 0.4) \times 10^{-3}$ ML s^{-1} and substrate temperatures of 300 and 350 K were chosen for the comparative study. In addition to the internal electron gun, the SPA-LEED system was equipped with an external e-gun. Therefore, it was possible to monitor the surface morphology during growth. After film growth, spot profiles were recorded under various scattering conditions with the internal gun.

3. STM measurements and internal faceting

For Cu on Ni(100), the most striking surface feature is a network of protruding stripes at coverages between 1 and 17 ML (see Fig. 1). The height of the stripes corresponds to one fourth to one third of the step height. These stripes appear even

a) $\Theta = 1$ ML

b) $\Theta = 6$ ML

c) $\Theta = 11$ ML
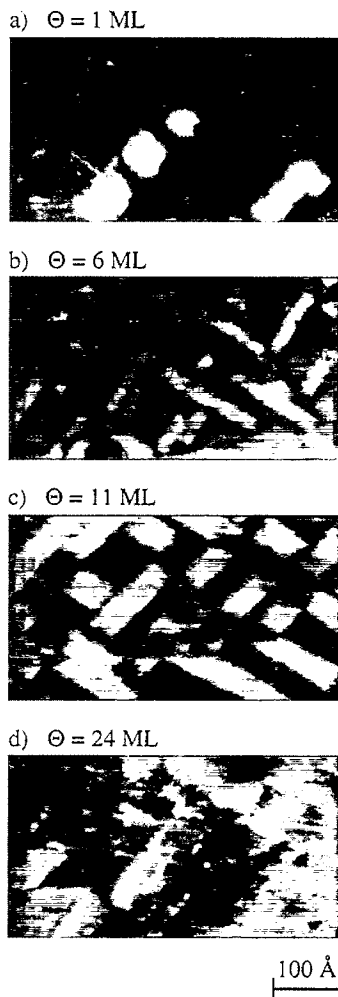

d) $\Theta = 24$ ML

|100 Å|

Fig. 1. Strain induced stripe pattern of epitaxial Cu films of different thickness on Ni(100) imaged by STM. The substrate temperature was 350 K and the deposition rates were 1.5×10^{-3} ML s^{-1} for (a)–(c), and 3.0×10^{-3} ML s^{-1} for (d). The STM images were recorded in differential mode (tunneling conditions: 5–8 nA, 0.5–1.5 V), which means that the derivative of the lines of constant current has been recorded and the images appear to be illuminated from the left.

for the submonolayer range ($\theta \cong 0.3$ ML), crossing islands which are larger than 60–80 Å (not shown). At monolayer coverage, the whole surface is covered by a network of stripes (Fig. 1a). The stripes are all running along $\langle 110 \rangle$ with equal probability for the two orthogonal domains. All stripes have a width of 5.5 ± 1.0 Å, which is the typical STM-imaging width of a single-atom chain [14]. Stripes shorter than 25 Å are not observed. This pattern is maintained up to coverages of about 20 ML (see Fig. 1b and Fig. 1c), while the width of the stripes increases stepwise with coverage. The average length, the density and the height of the stripes, however, remain constant above monolayer coverage [8,9].

The internal (111) faceting model, recently proposed [8,9], takes all of these experimental observations into consideration. The driving force of stripe formation is compressive strain between film and substrate, which is highest in the close-packed $\langle 110 \rangle$ directions. In the first monolayer, the film relieves the compressive strain by shifting rows of atoms from the fourfold hollow site to the twofold bridge site, whereby the rows are squeezed out of the film layer. The protruding atoms are staggered vis-a-vis the adjacent rows. They gain lateral freedom of expansion and the film can at least partially relieve its strain. Obviously, this lateral freedom of expansion compensates for any losses in binding energy.

The growth of the second layer on top of the protruding stripes leads to the formation of two atom wide chains. In the third layer, protruding stripes are three atoms wide, and so on. Consequently, the stripes formed in the first layer give rise to V-shaped structures in the film. Fig. 2 shows the situation for a 5-layer film. While the atoms, which do not belong to the V-shaped stripes (dark colored atoms) are expected to grow essentially pseudomorphically, the stripe atoms (light colored) can relieve strain at least perpendicular to the stripes. The network of stripes is stabilized by formation of highly stable close-packed internal {111} facets.

The model also explains why stripes never cross: perpendicular stripes are always separated by a half next neighbour distance (cp. Fig. 2).
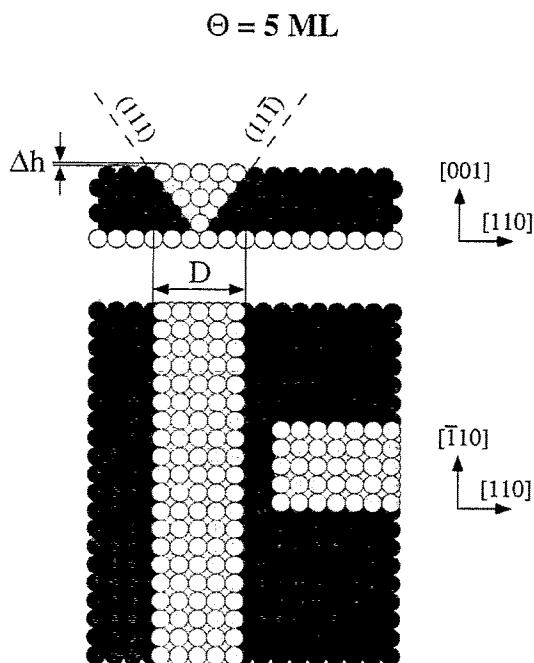
$\Theta = 5$ ML

Fig. 2. Internal (111) faceting model explaining the formation of the orthogonal stripe pattern. The open circles represent the substrate atoms (Ni). The "dark atoms" (Cu) are pseudomorphically placed at the fourfold hollow sites, whereby the stripe atoms (light colored) are placed at the twofold bridge sites in the first layer. As indicated, {111} facets are formed along the V-shaped stripe structures.

4. Diffraction studies

The diffraction pattern of Cu on Ni(100) contains only the fundamental substrate spots; no superstructure could be detected. The exact shape of the (00) spot for a 12 ML copper film on Ni(100) as seen by a two dimensional high-resolution scan is shown in Fig. 3. One can clearly see the satellites of the LEED spot orientated along $\langle 110 \rangle$. Since the satellites are very close to the (00) spot, the cross-like spot shape is obtained. The satellites of the LEED spot are caused by the pattern of stripes running along $\langle 110 \rangle$ (see Fig. 1).

By means of our SPA-LEED instrument, we were able to detect these satellites at coverages between 3 and 18 ML (substrate temperatures 300 K and 350 K). STM measurements showed the stripes to exist already at coverages of about 0.3 ML. This observation is not in disagreement
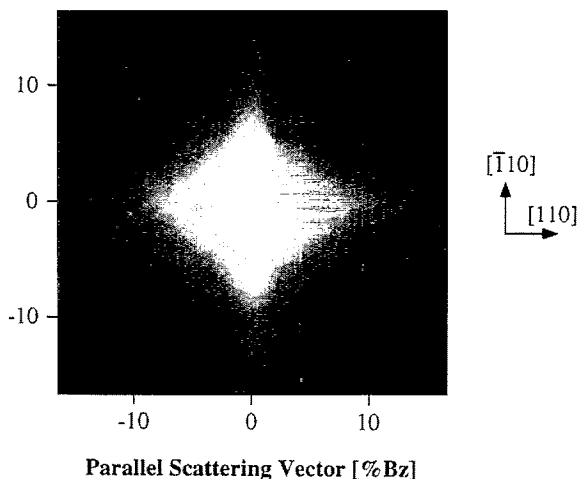
L. Nedelmann et al./Surface Science 376 (1997) 113–122

Θ = 12 ML

Parallel Scattering Vector [%Bz]

Fig. 3. High resolution LEED spot profile of the specular (00) beam taken from a 11.5 ML Cu film on Ni(100) grown at 350 K (deposition rate: 5×10^{-3} ML s^{-1}, electron energy: 43 eV, incidence angle: 7°). Note the characteristic cross-like shape of the spot with wings in $\langle 011 \rangle$ directions.

with the LEED measurements, since the *area covered* by the *stripes* has to reach about 10% to be detectable by LEED. The satellites become more and more pronounced as the film thickness increases and are best visible in the LEED pattern between 9 and 14 ML. At coverages above 18 ML, the LEED spots start to "blur out", until, at a coverage greater than 20 ML, only broad, isotropic spots occur, consistent with STM measurements. Above 17 ML, the stripe network vanishes. Fig. 1d shows the situation at a coverage of 25 ML: no stripes are visible and a dislocation network has formed.

The quantitative characterization of the stripe pattern is done by spot profile analysis. Quantities such as stripe density ρ, the fraction of the surface covered by stripes ϑ_s and the height of the stripes Δh can be extracted by means of this integral method. This is especially important concerning the stripe height, since STM images represent the electronic structure of a surface which is not necessarily equivalent to the atom position.

Spot profiles have been recorded parallel to $\langle 110 \rangle$ for diffraction patterns obtained at cover-

ages of 9.0 and 11.5 ML, where the satellites are well pronounced. The inset in Fig. 4 shows a typical spot profile. In addition to a constant background, one can distinguish between the following contributions:

(1) a central peak. Its full width at half maximum (FWHM) is given by the instrument and the mosaic broadening of the sample;

(2) satellites in the $\langle 110 \rangle$ directions. Their position does not change with scattering conditions;

(3) a broad shoulder due to inhomogeneities of the sample.

All parts of the spot profile were fitted using Lorentzian-like profiles $\kappa^2/(\kappa^2 + K_\parallel^2)^{3/2}$ with the help of a numerical least square fitting algorithm. This method allows us to determine unambiguously the intensity and the shape of the different contributions, even though – especially at higher scattering phases – the different contributions to the spot profile tended to "blur out" due to the mosaic spread of the sample, and discrimination seemed to be poor.
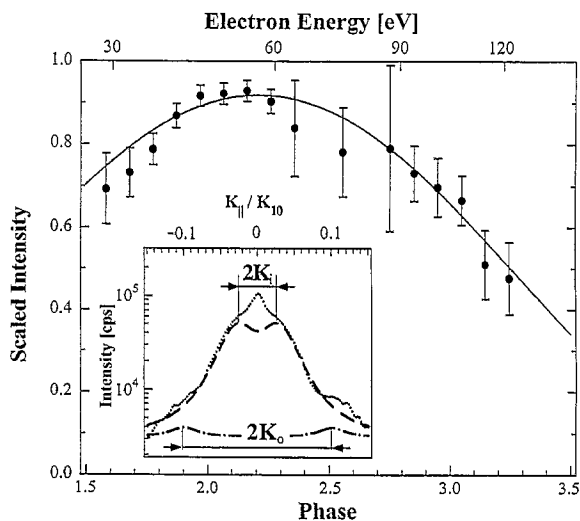

Fig. 4. LEED spot profile analysis (G(S) analysis) of a 11.5 ML Cu film on Ni(100) ($T_s = 300$ K, $R = 5 \times 10^{-3}$ ML s^{-1}). Inset: spot profile of the (00) spot at $S = 1.97$ along $\langle 110 \rangle$. For better clarity, the broad peak is subtracted from the experimental data (dots). Two pairs of satellites are clearly visible in the spot profile. The inner satellite pair is associated with the stripe separation, the outer with the stripe width. For G(S) analysis, see text.

The peak intensities vary considerably with the scattering phase due to dynamic multiple scattering effects, but the FWHM and the positions K_i and K_o of the satellites do not depend on electron energy. The position of the inner satellite K_i gives the mean distance ℓ between stripes: $\ell = 2\pi/|\mathbf{K}_i|$. We attributed the position of the outer satellite, K_o, to the width of the stripes D. The mean distance ℓ between stripes, which is independent of coverage and substrate temperature, determines the stripe density $\rho = \ell^{-2} = (7.3 \pm 1.5) \times 10^{-4}$ stripes per atom. This agrees nicely with the value found by STM: $\rho = (8.0 \pm 1.4) \times 10^{-4}$ stripes per atom.

The outer satellite is clearly visible in the experiments performed at the coverage of 11.5 ML. Its associated real space length, $D = 25 \pm 5$ Å = 10 ± 2 atoms, corresponds well with the width of the stripes. The internal faceting model gives an average stripe width of 11.5 atoms, in agreement with STM measurements ($D = 12 \pm 2$ atoms). The FWHM of the outer satellite is relatively small, indicating that there is only a small variation in the stripe width as expected from the internal faceting model and the STM measurements.

In order to perform a quantitative spot profile analysis one has to use the kinematic approximation taking into account only scaled intensities to get rid of dynamic effects [19]. By appropriate fitting procedures, the integral intensity of the central peak and the diffuse part, I_0 and I_d, are separated. Both the STM and the time-dependent SPA-LEED measurements (see below) have shown that multilayer films basically grow in step flow. Thus, the protruding stripes are the only relevant defect structures of the film and the effects on scattering from the few islands left at the surface can be neglected. Based on the kinematic theory for a two-level system [15], for such a stripe pattern the scaled integral intensity of the diffuse part can be written as:

$$\frac{I_d}{I_d + I_0} = 2\vartheta_s(1 - \vartheta_s)\left[1 - \cos\left(2\pi\frac{\Delta h}{d}S\right)\right]. \quad (1)$$

The equation describes the variation of the scaled intensity $I_d/(I_d + I_0)$ with the scattering phase S [16] within the kinematic approximation. The

scattering phase S, which is varied by changing the electron energy, is related to the height of a monatomic step. Since we consider the height of the stripes Δh, the factor $\Delta h/d$ has to be introduced. For the quantitative analysis of the stripe height Δh and the fraction of the surface covered by stripes ϑ_s, Eq. (1) is used. I_d is given by the integral intensity of the inner satellite and I_0 corresponds to the integral intensity of the central peak. Fig. 4 shows an example for the evaluation of the integral intensity as function of the scattering phase. All measured curves show a maximum close to $S = 2$, so that the ratio $\Delta h/d$ equals 1/4. A more precise value is obtained by fitting the experimental data to Eq. (1). The two fitting parameters, $\Delta h/d$ and ϑ_s, correspond to 0.235 ± 0.010 and 0.32 ± 0.03, respectively. Using the step height $d = 1/2 \times 3.61$ Å, the height of stripes Δh is found to be 0.42 ± 0.02 Å. By the use of $D = 10 \pm 2$ atoms, $\rho = (7.3 \pm 1.5) \times 10^{-4}$ per atom and $\vartheta_s = 0.32 \pm 0.03$, one finds the mean length of the stripes $\bar{s} = 35.5 \pm 15.0$ atoms.

The results of the G(S) analysis are in perfect agreement with the internal faceting model as well as with the STM measurements. The simple hard sphere model predicts a stripe height of 0.40 Å, a value which is also obtained by G(S) analysis ($\Delta h = 0.42 \pm 0.02$ Å). Even the STM gives a reasonable value ($\Delta h = 0.6 \pm 0.1$ Å). This cannot necessarily be expected, since height measurements by STM are not only determined by geometrical factors but also by electronic contributions [17,18].

Above 20 ML, the network of stripes vanishes and a dislocation network is observed by STM. The surface resembles a patchwork of tilted microterraces. Quantitatively, this tilt can be described by the mosaic spread. The standard variation of the angular distribution of mosaic spread is denoted here as mosaic angle ϕ_θ. In diffraction, the mosaic spread causes a broadening of the Bragg rods into cone-shaped bunches. That means, the FWHM of the spot profiles increases with the scattering phase S [19]:

$$\text{FWHM}(\theta) = \frac{a}{d}\tan\phi_\theta S, \quad (2)$$

where a and d are the lateral lattice constant and

the interlayer distance, respectively. For fcc(100) surfaces, one finds $a/d = \sqrt{2}$.

The plot of FWHM versus S at a coverage of 25 ML is displayed in Fig. 5. The total mosaic angle corresponds to $\phi_{25} = 1.48 \pm 0.05°$. One has to substract the mosaic angle of the substrate ($\phi_0 = 0.16 \pm 0.02°$) [20]. Thus, the mosaic angle ϕ inherent to the copper film and caused by the dislocations is $\phi = 1.32 \pm 0.07°$. Supposing a monatomic height for each dislocation, one obtains a dislocation density ρ_D of $(10.6 \pm 1.0) \times 10^{-4}$ per atom. This value is comparable to the density of stripes ρ which is found at intermediate coverages ($\theta = 1$–17 ML).

5. Growth kinetics

STM measurements have shown that copper on Ni(100) grows in the first two monolayers in a layer-by-layer fashion and above a coverage of 2 ML even in the step flow mode. This is also evident from Fig. 6, which shows the peak intensity of the (00) spot at out-of-phase condition ($S = 1.55$) as a function of coverage during growth. Intensity oscillations are present during the growth

(a) Intensity Oscillations during Growth
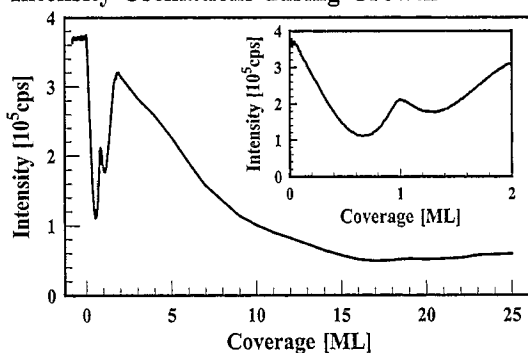
(b) Spot Profiles
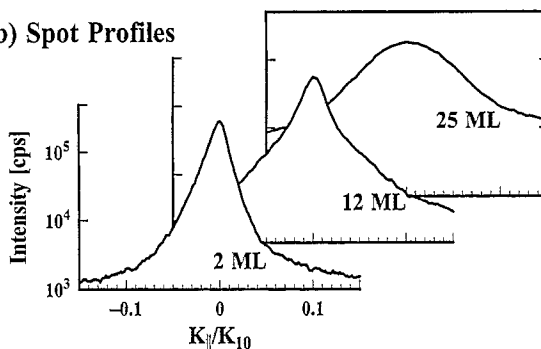
Fig. 6. (a) Evolution of the peak intensity of the (00) LEED spot during epitaxial growth of Cu on Ni(100). ($T_s = 350$ K, $R = 5 \times 10^{-3}$ ML s^{-1}). The first two layers' oscillations are related to 2D islands. Above 2 ML, the film grows in the step flow mode and the attenuation of the peak intensity is only caused by the increasing stripe coverage. (b) Evolution of the LEED spot profiles during growth. Due to the stripes, satellites appear at low coverages while the whole spot is dramatically broadened for thick films containing dislocations.

of the first two monolayers. Note, the intensity minimum at $\theta \cong 0.7$ ML is pronounced and the first maximum at $\theta = 1$ ML weak. This is consistent with the STM results which show the highest saturation island density in the first layer and the onset of nucleation in the second layer starting before the first layer is completed (see Ref. [8] and Fig. 1a). At coverages above 2 ML no oscillations occur, the intensity decreases uniformly. This means, for coverages $\theta > 2$ ML, we do not observe island formation within the transfer width of the SPA-LEED instrument. Usually one expects constant peak intensity for the step flow mode. Here, however, the intensity is attenuated by the
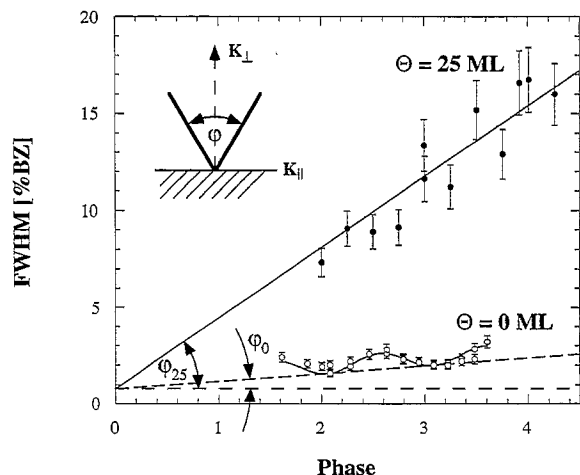

Fig. 5. Determination of the mosaic spread for a 25 ML Cu film on Ni(100). For the substrate, a superposition of linear increase of the FWHM due to the mosaic spread $\phi_0 = 0.16°$ (dashed line) and oscillations due to atomic steps are detected. The formation of dislocations for a 25 ML film yields a dramatic increase of the mosaic spread $\phi = 1.32°$ (solid line).

destructive interference between the elevated stripes and the terraces.

This observation is again in agreement with the STM measurements (see Fig. 1). Island densities in the first and in the second layer are elevated and correspond to a mean island separation of 100–150 Å. At higher coverages we found only few islands on large terraces, with an island separation greater than 600 Å. Because the average terrace width is smaller, the film grows in step flow and one detects only flat terraces.

The increased island density in the first Cu layers is of kinetic origin. While at the submonolayer level the nucleation kinetics are determined by the Cu–Ni interaction, with increasing film thickness the film adopts more and more a copper-like behaviour, so that finally the nucleation kinetics will resemble those of Cu/Cu(100). For both Cu on Cu(100) and Cu on Ni(100), the migration barrier E_m, the dimer bond energy E_b and the size of the critical nucleus have been determined [21,22]. The migration barriers are equal within the error bars, 0.35 ± 0.02 eV (Ni(100)) [22] and 0.36 ± 0.03 eV (Cu(100)) [21], while, surprisingly, the dimer bond energies differ considerably, (0.46 ± 0.19) eV (Ni(100)) [22] as against 0.04 ± 0.03 eV (Cu(100)) [21]. The tetramer is the smallest stable island at room temperature in both cases. For that the saturation island density n_x is given by $n_x \propto \exp[(1/5kT)(3E_m + 2E_b)]$ using mean field nucleation theory [24]. As the migration barriers for Cu on Cu(100) and Cu on Ni(100) are nearly identical, the substantial difference in the dimer bond energy is the physical reason for the coverage dependent island density. Indeed, assuming a critical island size of 3 and $E_m = 0.35$ eV, a difference of the bond energy by a factor of 10 results in a difference in the island densities of more than two orders of magnitude, in fair agreement with the experimental observation.

The evolution of spot profiles during growth is reported in Fig. 6b; the results of the quantitative spot profile analysis are shown in Fig. 7. The spot profiles were fitted numerically, and we can describe them as a superposition of a central peak and two satellites. In the fitting procedure, the FWHM of the central peak was chosen to be
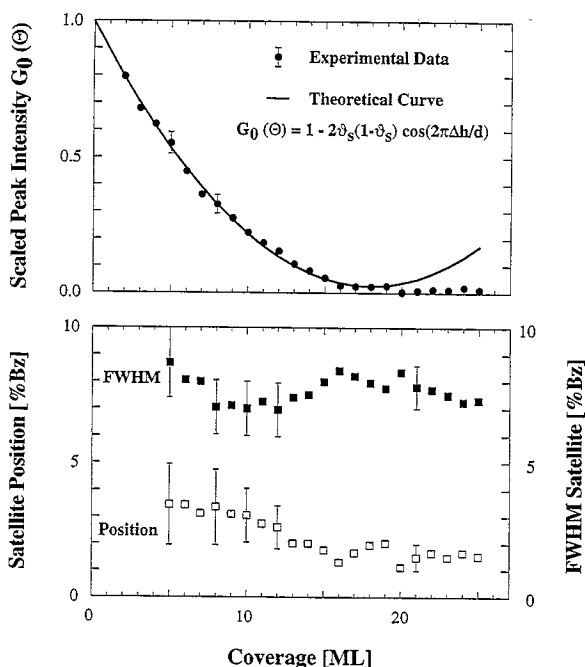

Fig. 7. (a) Quantitative description of peak intensity of the central LEED peak versus coverage. From the minimum of the parabola one deduces that half of the copper film is covered by stripes at 18 ± 1 ML. (b) Evolution of the satellite FWHM and the position with coverage.

constant. The FWHM of the satellites does not change markedly with the coverage (see Fig. 7b). Since the scattering phase is rather low ($S = 1.55$), the sensitivity for mosaic broadening is relatively weak in this experiment. At a higher scattering phase, one finds a broadening of the FWHM with increasing coverage. For coverages up to 17 ML the satellites seem to move towards the central peak with coverage. However, as this tendency is weak and within the limit of experimental error, no definite conclusions can be drawn. Concerning the scaled intensity of the central peak $I_0/(I_0 + I_d)$, one expects a decrease with coverage θ according to a square law:

$$G_0(\theta) = \frac{I_0}{I_0 + I_d} = 1 - 2\vartheta_s(1 - \vartheta_s)\cos(2\pi\Delta h/d).$$

$$(3)$$

This expression is equivalent to Eq. (1), but here the integral intensity of the central peak

instead of the diffusive part is considered. ϑ_s is given by the film thickness θ, $\vartheta_s = \vartheta_1 \times \theta$, where ϑ_1 is one of the parameters to be fitted. The minimum of the parabola given by Eq. (3) indicates that the surface is half covered by stripes ($\vartheta_s = 0.5$). Indeed, the experimental data fulfil such a law, the minimum corresponds to $\theta = 18 \pm 1$ ML. This value is in good agreement with the spot profile analysis. Extrapolating the stripe coverage obtained from the G(S) analysis for 11.5 ML one expects a stripe coverage of 50% at a film thickness of 18 ± 3 ML assuming the linear increase of the stripe coverage with copper coverage. STM predicts a value of 15.5 ± 2.0 ML [8].

At coverages greater than 18 ML ($\vartheta_s > 0.5$) the central peak intensity does not increase again as expected from Eq. (3), but stays more or less constant. Apparently, the strain relief mechanism via internal faceting is not efficient for coverages above 18 ML. This is also supported by the disappearance of the cross-like shape of the LEED spots at this coverage. From 18 ML onwards strain is no longer relieved via internal facets but by the formation of dislocations. This leads to surface structures as shown in Fig. 1d and described quantitatively in Fig. 5.

It should be mentioned that the diffraction pattern of Cu submonolayers cannot be analyzed using the simple kinematic approximation because of the different form factors of the Ni substrate and the Cu adlayer (multiple scattering). For the scattering condition used here, however, the difference between the two form factors cannot be larger than 7% as obtained by extrapolating the intensity for Cu multilayers to $\theta = 0$ ML (cf. Fig. 6). The shift of the first minimum from $\theta = 0.5$ ML to $\theta \cong 0.7$ ML is also due to a difference of the two form factors [23]. Nevertheless, the kinematic approximation for the spot profile analysis used in Figs. 4 and 7 is still valid since above monolayer coverage the surface is completely Cu terminated.

In addition, Cu/Ni(100) can indeed be described as a two-level system, an assumption upon which the spot profile analysis according to Eq. (1) is based. LEED measurements during growth reveal that this assumption is fulfilled at a substrate temperature of 350 K since the decrease in peak intensity is fully explained by the growth of the stripe pattern as given by Eq. (1).

6. Conclusion

STM and SPA-LEED are complementary surface sensitive techniques. Both methods have been used for the quantitative analysis of the surface morphology of epitaxial copper films on Ni(100). The compressive strain, resulting from the atomic size mismatch of 2.6% between Cu and Ni, is relieved by the formation of V-shaped defects with {111} facets in the Cu film. This strain relief mechanism gives rise to a characteristic pattern of orthogonal stripes at the film surface. In the first monolayer, monatomic chains of Cu atoms are shifted laterally from the fourfold hollow configuration to the twofold bridge configuration and thereby protrude from the surface layer. The gain in lateral freedom of expansion of the protruding atoms compensates for their lowered binding energy. With each Cu layer added the relaxed stripes grow in width by one atom, forming internal {111} interfaces in the Cu film. In this mode the film grows layerwise up to about 18 monolayers where bulk dislocations are formed through merging stripes.

The stripe pattern is an interesting subject to elucidate the respective advantages of STM and LEED. Cu on Ni(100) represents a nearly ideal two level system; islands can be neglected for the quantitative analysis of the stripe pattern. The present study shows that both methods yield the same values for the stripe width, the density of the stripes and the fraction of the surface covered by the stripes. Even for the height of the stripes the agreement between STM and LEED is quite good, although electronic contributions may influence the STM result.

STM is a local probe method giving unprecedented microscopic insights in growth phenomena. Its unique potential to explore kinetic surface processes such as adatom diffusion, nucleation and aggregation on the atomic scale has allowed the testing of microscopic theories of film growth and stimulated new developments. Reciprocal space methods can also give access to atomistic growth

processes, but their application does have certain disadvantages. We briefly illustrate this point for the example of nucleation of islands in the initial phase of epitaxial growth [25]. With STM it is straightforward to obtain a real space view of nucleation, count the island density, measure the island size distribution or determine the average island separation. Diffraction techniques, on the other hand, have difficulties in characterizing islands at small coverage (<0.1 ML). In addition, they require a certain preknowledge about island size and separation distributions in order to extract distances and densities in real space. In contrast to local probe methods, the averaging character of reciprocal space techniques yields a high statistical significance, yet at the same time it can be a disadvantage since areas with defects such as substrate steps are included in the average.

The situation is reversed concerning the structural analysis of epitaxial films. STM quite often provides a qualitative picture but the quantitative analysis is difficult. An example is the determination of step heights. STM has difficulties due to electronic contributions which can distort the determination of surface morphology. A prominent example is the imaging of Ag islands on the Pt(111) surface [18]. Although the atomic size of Ag at 2.89 Å is only 0.12 Å larger than that of Pt, a Ag island is imaged 0.6 Å higher than a corresponding Pt island on the Pt(111) surface. With diffraction techniques, on the other hand, the determination of height differences is straightforward. Only at complex surfaces is the interpretation of diffraction experiments not necessarily singlevalued, demanding a careful analysis. The qualitative picture provided by STM can offer a valuable starting point. In any case the major advantage of integrating reciprocal space techniques is their high statistical significance which yields numerical results with high precision. In addition, diffraction techniques can provide data which are often not accessible by local probe methods such as STM. For example, the evaluation of mosaic angles is straightforward with SPA-LEED as has been shown in the present study.

A definite advantage of the diffraction technique is also its "real-time" capability. Despite considerable efforts, in situ measurements during growth at "technologically relevant" MBE growth rates of up to 1 ML s^{-1} are not yet possible by STM. At best, video rates of about one image (size: 1000 Å × 1000 Å) per minute are obtained [26]. SPA-LEED, on the other hand, has no such constraints: it is well suited to determine the growth mode recording the specular intensity since detection rates up to 1 kHz are achieved. Individual spot profiles during deposition can be measured with frequencies up to 2 Hz.

Local real space microscopy and integrating reciprocal space diffraction experiments are largely complementary techniques. The synergism between the two experimental approaches allows a comprehensive characterization of epitaxial growth phenomena.

References

[1] J. Villain, A. Pimpinelli, L. Tang and D. Wolf, J. Phys. (Paris) 2 (1992) 2107.
[2] F.C. Frank and J.H. van der Merwe, Proc. Roy. Soc. A 198 (1949) 2168.
[3] J.W. Matthews and A.E. Blakeslee, J. Cryst. Growth 27 (1974) 118.
[4] M.A. Grinfeld, Sov. Phys. Dokl. 31 (1986) 831.
[5] H. Brune, H. Röder, C. Boragno and K. Kern, Phys. Rev. B 49 (1994) 2997.
[6] C. Günther, J. Vrijmoeth, R.Q. Hwang and R.J. Behm, Phys. Rev. Lett. 74 (1995) 754.
[7] M. Henzler, C. Homann, U. Malaske and J. Wollschläger, Phys. Rev. B 52 (1995) 17060.
[8] B. Müller, B. Fischer, L. Nedelmann, A. Fricke and K. Kern, Phys. Rev. Lett. 76 (1996) 2358.
[9] B. Müller, L. Nedelmann, B. Fischer, A. Fricke and K. Kern, J. Vac. Sci. Technol. A 14 (1996) 1878.
[10] S.A. Chambers, H.W. Chen, I.M. Vitomirov, S.B. Anderson and J.H. Weaver, Phys. Rev. B 33 (1986) 8810.
[11] A. Chambers and D.C. Jackson, Philos. Mag. 31 (1975) 1357.
[12] H. Brune, H. Röder, K. Bromann and K. Kern, Thin Solid Films 264 (1995) 230.

[13] U. Scheithauer, G. Meyer and M. Henzler, Surf. Sci. 178 (1986) 441.

[14] Monoatomic Cu chains are usually imaged with a width of ∼5–8 Å, J.P. Bucher, E. Hahn, P. Fernandez, C. Massobrio and K. Kern, Europhys. Lett. 27 (1994) 473.

[15] C.S. Lent and P.I. Cohen, Surf. Sci. 139 (1984) 121.

[16] The scattering phase $S = (K_\perp d)/(2\pi) = (1/h)2d\sqrt{2m_e E}\cos\alpha$ is varied by changing the electron energy E. Here, $d = 1.8$ Å is the height of a monatomic step, $K_\perp$ denotes the vertical component of the scattering vector, h is Planck's constant, m_e the electron mass and α the angle of incidence.

[17] Y.W. Mo and F.J. Himpsel, Phys. Rev. B 50 (1994) 7868.

[18] H. Röder, R. Schuster, H. Brune and K. Kern, Phys. Rev. Lett. 71 (1993) 2086.

[19] M. Henzler, Defects at Surfaces, Springer Series in Surface Science, Vol. 3, Eds. F. Nizzoli, K.H. Rieder and R.F. Willes (Springer, Berlin, 1984) p. 14.

[20] In the case of the clear sample, the linear increase of the FWHM is superimposed by oscillations due to the finite terrace length. A more complete analysis is needed to fully describe the behaviour of such a curve, it yields an average terrace length Γ of 158 ± 15 Å. For details, see e.g. E.Z. Luo, S. Henn, M. Kennedy, J. Wollschläger and M. Henzler, Phys. Rev. B 49 (1994) 4858.

[21] J.K. Zuo, J.F. Wendelken, H. Dürr and C.L. Liu, Phys. Rev. Lett. 72 (1994) 3064;
H. Dürr, J.F. Wendelken and J.K. Zuo, Surf. Sci. 328 (1995) L527.

[22] B. Müller, L. Nedelmann, B. Fischer, H. Brune and K. Kern, Phys. Rev. B, accepted for publication.

[23] J. Wollschläger and A. Meier, Appl. Surf. Sci. 104/105 (1996) 392.

[24] J.A. Venables, G.D.T. Spiller and M. Hanbücken, Rep. Prog. Phys. 47 (1984) 399.

[25] H. Brune, H. Röder, C. Boragno and K. Kern, Phys. Rev. Lett. 73 (1994) 1955.

[26] U. Köhler, L. Andersohn and B. Dahlheimer, Appl. Phys. A 57 (1993) 491.